

# Can inducing the Crow instability reduce contrail radiative forcing?

By T. Ferreira\*, D.-G. Caprace\*†, R. Paoli‡, K. Shariff‡, AND S. K. Lele

We perform time-developing simulations of an aircraft plume in a stratified atmosphere to assess whether artificially inducing the Crow instability of trailing vortices via out-of-phase deflection of two ailerons on each wing (so as to maintain a constant lift) can reduce contrail radiative forcing. The initial condition consists of (i) a vortex sheet with a longitudinally varying strength to mimic the effect of aileron deflection, (ii) warm vapor-laden jets that are initially perturbed and (iii) Lagrangian particles in the jets that subsequently grow due to ice deposition. Separate simulations are performed with the compressible charLES code and the incompressible Vortex Particle-Mesh (VPM) method. Radiative forcing is assessed using a parameterization in terms of optical depth. We find that, for a range of surface albedos and zenith angles of the sun, particle redistribution by the forced Crow instability leads to an increased radiative forcing compared to a control case where the instability develops naturally.

---

## 1. Introduction

The goal of this work is to assess whether artificially inducing the Crow (1970) instability of aircraft trailing vortices can reduce the radiative forcing (RF) of the associated line-shaped contrail and the ensuing contrail cirrus. It has been estimated that contrail cirri have a net warming effect greater than that due to aviation CO<sub>2</sub>, albeit with a large uncertainty (Lee *et al.* 2021). These estimates of contrail RF are obtained by running global climate models (Bock & Burkhardt 2016; Bickel *et al.* 2020) on a flight inventory.

Contrail warming arises because, on average, contrails absorb more longwave (infrared) radiation from the ground than they reflect shortwave solar radiation. This suggests that, if one were able to induce gaps to form in a contrail plume, then longwave absorption would be reduced. In other words, the goal is to reduce the ice column density [called the ice water path (IWP)] in certain regions, which would increase IWP in other regions. If the latter regions were optically thick to begin with, so that most of the absorption occurred in a thin vertical layer, then an increased IWP would not lead to any greater absorption in the IWP-dense regions. Thus, a net reduction in longwave absorption would result. The gaps are to be created by oscillating ailerons to induce the Crow instability of a pair of trailing vortices. The instability culminates in a cross-linking of the two rolled-up wake vortices and the formation of separated ring-like vortices. The majority of airliners have two or more ailerons on each wing that can be oscillated 180° out of phase so as not to change the total lift and rolling moment. A similar mechanism was proposed by Crouch *et al.* (2001) to accelerate the demise of wake vortices of aircraft on approach. Lewellen & Lewellen (2001) hypothesized that any change in Crow instability dynamics would impact the contrail dispersion, vertical mixing and ice crystal number.

\*These authors contributed equally to the work.

† NASA Ames Research Center

‡ Department of Mechanical Engineering, Polytechnique Montréal, Canada

## 2. Methods

### 2.1. Vortex sheet distribution that mimics aileron oscillation

We adopt the following convention for coordinates:  $x$  is streamwise,  $y$  is spanwise and  $z$  is vertical. According to lifting line theory (Batchelor 1967, p. 583), a wing spanning the interval  $y \in [-b/2, b/2]$  produces a vortex sheet with streamwise vorticity having the strength

$$\gamma(y) = -d\Gamma(y)/dy, \quad (2.1)$$

where  $\Gamma(y)$  is the bound circulation of the wing. We assume an elliptically loaded wing for which

$$\Gamma(y) = \Gamma_0 \left(1 - y^2/b^2\right)^{\frac{1}{2}}, \quad (2.2)$$

where  $\Gamma_0$  is the circulation at midspan also equal to the circulation of the trailing vortices. The lift  $L$  is obtained as the integral of the sectional force derived from the bound circulation using the Kutta-Joukowski theorem

$$L = \rho U \Gamma_0 b_0, \quad (2.3)$$

where  $U$  is the flight velocity and  $b_0 = b\pi/4$  is the spacing between the rolled-up vortices.

A lift-preserving perturbation of the sheet strength is introduced to model aileron deflection

$$\begin{aligned} \gamma_{\text{ail}}(y) = \Gamma_{\text{ail}} \left[ \right. & (\delta(y - y_{i,l}) - \delta(y - y_{i,r}) - \delta(y + y_{i,l}) + \delta(y + y_{i,r})) \\ & \left. - \frac{(y_{i,r} - y_{i,l})}{(y_{o,r} - y_{o,l})} (\delta(y - y_{o,l}) - \delta(y - y_{o,r}) - \delta(y + y_{o,l}) + \delta(y + y_{o,r})) \right], \end{aligned} \quad (2.4)$$

where  $\delta$  is the Dirac delta function,  $\Gamma_{\text{ail}}$  is the circulation of the inner aileron vortex and  $y_{i,l}, y_{i,r}, y_{o,l}, y_{o,r}$  are the spanwise locations of the aileron edges. The subscripts may be read as  $i$  for inboard,  $o$  for outboard,  $l$  for left and  $r$  for right. This perturbation is applied to one case only (hereafter referred to as forced), whereas, in the baseline case,  $\gamma_{\text{ail}} = 0$ . Note that this has nothing to do with the randomness introduced in the jet, which is present in both cases (cf. Section 2.2).

The vortex sheet is regularized so that it can be discretized and captured on the simulation grid. The vorticity is obtained as the convolution of the singular sheet distribution with a Gaussian kernel,

$$\omega(\mathbf{x}) = \frac{1}{b} \int_{-b/2}^{b/2} \left( \gamma(y') + \sin\left(2\pi \frac{x}{L_x}\right) \gamma_{\text{ail}}(y') \right) \frac{1}{\pi\sigma^2} \exp\left(-\frac{((y-y')^2 + z^2)}{\sigma^2}\right) dy', \quad (2.5)$$

with  $\sigma$  a smoothing length (given in Table 1) and  $L_x$  the streamwise domain length. Note that the temporal deflection of ailerons is represented by a sinusoidal modulation of  $\gamma_{\text{ail}}(y)$  along the streamwise coordinate  $x$ . The velocity and pressure fields are derived similarly using the corresponding Green's function associated with the Gaussian kernel.

### 2.2. Engine exhaust jet

A pair of jets is added to the initial condition at the same height as the vortex,  $z_j = 0$ , at spanwise locations  $y = \pm y_j$ , with a Gaussian axial velocity profile,

$$u_x(r) = u_j \exp\left(-\frac{4r^2}{R_j^2}\right), \quad (2.6)$$

with  $r^2 = (y - y_j)^2 + z^2$ . The jets are also associated with a local increase in temperature and absolute humidity following the same radial profile. The temperature, water vapor mass fraction and velocity within the jet are randomly perturbed by 20% of their difference with the ambient values. Lagrangian tracers are initialized in the jet that track the growth of ice crystals following the microphysics model described in the next section. Their number density is also prescribed to follow the same radial profile.

### 2.3. Microphysics

The simplified microphysical scheme of Paoli *et al.* (2013) is employed to model the growth of ice on a number  $N_p$  of initially ice-activated particles. The more sophisticated microphysical scheme used in Bier *et al.* (2022) has been implemented and may be used in future studies. Each Lagrangian tracer represents a multiple  $M_p$  of actual ice particles. Ice particle growth leads to a depletion of atmospheric humidity, and this is captured through a sink term in the conservation equation for vapor mass. Latent heat release in the flow due to freezing is neglected (since the associated temperature changes are negligible compared to buoyancy-induced changes), as well as any transfer of momentum between the particles and the flow. Ice crystal coagulation is not modeled at this stage.

### 2.4. Codes

Throughout this work, we use two distinct codes and compare their results, as follows.

charLES: computational fluid dynamics (CFD) code from Cadence (previously Cascade Technologies, Inc.), a 3D massively parallel, unstructured, cell-centered finite volume, compressible flow solver (Ham *et al.* 2006). This solver uses a second-order central scheme for the space discretization of the carrier phase and an explicit three-stage Runge-Kutta method for the time discretization for both carrier and disperse phases.

VPM method: a hybrid Lagrangian-Eulerian CFD solver that operates on the vorticity-velocity formulation of the Navier-Stokes equations and treats stratification using the Boussinesq approximation. This method uses Lagrangian particles to treat vorticity advection. Vorticity diffusion, stretching and subgrid scale model are implemented using fourth-order finite differences evaluated on a background Cartesian grid. A Fourier-based solver is used to compute the velocity from the vorticity. Information is passed back and forth between the particles and the grid through high-order interpolation (Chatelain *et al.* 2008).

### 2.5. Simulation parameters

Simulation parameters are mostly based on the large-eddy simulation (LES) work of Naiman (2011) on the vortex phase of contrails. We set the peak value of the water vapor mass fraction in the jet to match the temperature-vapor mixing line assumption from the Schmidt-Appleman criterion for contrail formation (Appleman 1953). Starting from set atmospheric conditions, we derive this value based on an overall propulsive efficiency  $\eta_{\text{prop}}$  of 35% and assuming the same jet peak temperature 224.4 K as in Naiman (2011). The atmospheric and aircraft parameters are summarized in Table 1. Stratification is applied following the work of Paoli *et al.* (2013). Due to the different incompressible and compressible nature of the codes, the boundary conditions and the meshing differ across their simulations, as described in Table 2.

Atmospheric parameter	Value
Ambient temperature at aircraft altitude, $T_0$ [K]	220
Ambient pressure at aircraft altitude, $p_0$ [hPa]	240
Ambient density at aircraft altitude, $\rho_0$ [kg m <sup>-3</sup> ]	0.38
Ambient water vapor mass fraction at aircraft altitude, $Y_0$	$8.94 \times 10^{-5}$
Brunt-Väisälä frequency, $N_{BV}$ [s <sup>-1</sup> ]	0.015
Constant ambient relative humidity over ice, $RH_i$ [%]	130
Aircraft parameter	Value
Aircraft wingspan, $b$ [m]	47.2
Trailing vortex circulation, $\Gamma_0$ [m <sup>2</sup> s <sup>-1</sup> ]	390
Inner aileron vortex circulation, $\Gamma_{ail}$ [m <sup>2</sup> s <sup>-1</sup> ]	$0.1\Gamma_0$
Sheet smoothing length scale, $\sigma$ [m]	1.5
Aileron edge positions, $y_{i,l}, y_{i,r}, y_{o,l}, y_{o,r}$ [m]	$0.15b, 0.19b, 0.38b, 0.50b$
Jet radius, $r_j$ [m]	3.3
Jet spanwise location, $y_j$ [m]	12.2
Streamwise velocity at jet center, $u_j$ [m s <sup>-1</sup> ]	14.0
Temperature at jet center, $T_j$ [K]	224.4
Water vapor mass fraction at jet center, $Y_j$	$2.87 \times 10^{-4}$
Number of computational particles per jet per meter of plume, $N_p/L_x$ [m <sup>-1</sup> ]	$5.40 \times 10^4$
Superparticle multiplier, $M_p$	$2.73 \times 10^8$

TABLE 1. Atmosphere and aircraft parameters.

Parameter	charLES	VPM
Domain dimensions, [m <sup>3</sup> ]	$8b_0 \times 40b_0 \times 60b_0$	$8b_0 \times 8b_0 \times 8b_0$
Refinement region dimensions, [m <sup>3</sup> ]	$8b_0 \times 4b_0 \times 12b_0$	$8b_0 \times 8b_0 \times 8b_0$
Streamwise resolution, $\Delta_x$ [m]	1.54	0.77
Cross resolution, $\Delta_y = \Delta_z$ [m]	0.77	0.77
Streamwise boundary conditions	periodic	periodic
Spanwise boundary conditions	periodic	unbounded
Vertical boundary conditions	inlet/outlet	unbounded

TABLE 2. Parameters for the mesh and boundary conditions.

### 3. Radiative forcing parameterization

We employ the parameterization of RF in terms of the shortwave optical depth developed for clouds by Corti & Peter (2009) and used by Sanz-Morère *et al.* (2021) for overlapping contrails. For conciseness, we only provide the final expressions for short- and longwave RF. The former is

$$\text{RF}^{\text{SW}} = -S 0.73(1 - \alpha) \frac{R_c - \alpha R'_c}{1 - R'_c}, \quad R_c \approx \frac{\tau / \cos \theta}{7.7 + \tau / \cos \theta}, \quad R'_c = \frac{2\tau}{7.7 + 2\tau}, \quad (3.1)$$

with  $\tau$  the optical depth,  $\alpha$  the surface albedo,  $S \equiv 1366.1 (1 + 0.033 \cos(2\pi J/365)) \cos \theta$  the solar flux,  $\theta$  the solar zenith angle and  $J$  the Julian day taken as 152 (June 1<sup>st</sup>). The latter reads,

$$\text{RF}^{\text{LW}} = \epsilon \sigma^* (T_{\text{surf}}^{2.528} - T_{\text{cloud}}^{2.528}), \quad \epsilon = \alpha \approx 1 - \exp(-0.75\tau), \quad (3.2)$$

where  $\sigma^* = 1.607 \times 10^{-4} \text{ W m}^{-2} \text{ K}^{-2.528}$  is an effective Stefan-Boltzmann constant.

The contrail optical depth  $\tau(x, y)$  is obtained as a function of the spanwise and the streamwise coordinates of the plume. The ice particles in the 3D computation are partitioned into vertical columns of size  $\Delta x \times \Delta y$ , the union of which covers the entire horizontal plane. The optical depth of a given column is computed as an integral along

	Unstratified	Stratified
No jets	$\lambda_{\text{obs}} = 8b_0$	$\lambda_{\text{obs}} = 4b_0$
With jets	$\lambda_{\text{obs}} = 8b_0$	$\lambda_{\text{obs}} = 4b_0$ ( $= 8b_0$ if $b_0 = 0.82b$ )

TABLE 3. Results of the observed wavelength  $\lambda_{\text{obs}}$  for a pair of straight and randomly perturbed Lamb-Oseen vortices.

the vertical direction that, for the case of  $N_{\text{vert}}$  discrete particles in the column, yields

$$\tau(x, y) = \sum_{p=1}^{N_{\text{vert}}} \frac{\pi r_p^2}{\Delta x \Delta y} Q_{\text{ext}}(r_p), \quad (3.3)$$

with  $r_p$  the radius of the ice particle. The Mie extinction coefficient  $Q_{\text{ext}}$  is approximated according to van de Hulst (1981),

$$Q_{\text{ext}} = 2 - \frac{4}{\rho} \left( \sin(\rho) - \frac{1 - \cos(\rho)}{\rho} \right), \quad \rho \equiv \frac{4\pi r_p (\mu - 1)}{\lambda}, \quad (3.4)$$

and we choose a refractive index of  $\mu = 1.31$  and a light wavelength of  $\lambda = 0.55 \mu\text{m}$  [as proposed by Kärcher *et al.* (2009)].

To enable a numerical comparison between different line-shaped contrails, we report the radiative effect (RE) per contrail length (in W/m), which is the integral of the RF (both short- and longwave) in the spanwise direction, and averaged in the longitudinal direction,

$$\text{RE} = \frac{1}{L_x} \int_0^{L_x} \int_0^{L_y} (\text{RF}^{\text{SW}}(x, y) + \text{RF}^{\text{LW}}(x, y)) \, dx \, dy. \quad (3.5)$$

## 4. Results

### 4.1. Vortex pair instability wavelength

For the case of a vortex sheet that is initially perturbed (forced) at the Crow instability wavelength of  $8b_0$ , we observed the same wavelength in the plume at a later time. However, for the baseline (unforced) sheet with only random perturbations in the jet, we observed half the Crow wavelength with both codes. To understand the origin of this difference, we replaced the vortex sheet with Lamb-Oseen (LO) vortices, varied the mesh resolution and vortex core radius and ran cases with and without stratification and jets. An initial random perturbation was applied to the LO vortices in the absence of jets. The results of this study, summarized in Table 3, were consistent across the two codes.

From the table, we see that the Crow wavelength is obtained for the unstratified cases with and without jets. For the stratified cases, we observed half the Crow wavelength, except when, following Naiman (2011), we set the vortex spacing to be  $b_0 = 0.82b$  rather than the elliptic loading value of  $b_0 = b\pi/4 \approx 0.79b$ . At this stage of the work, the cause for the appearance of half the Crow wavelength for baseline, non-forced sheets and vortices is still unclear. The classical calculation of the most unstable wavelength, as reviewed by Leweke *et al.* (2016), was established for unstratified conditions. Although

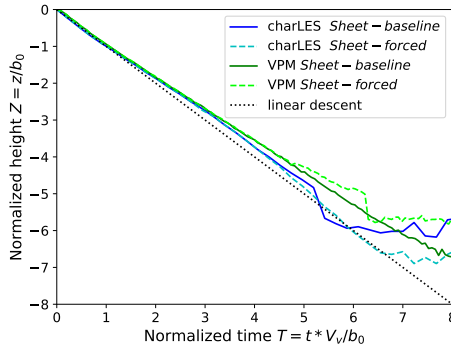


FIGURE 1. History of vortex rate of descent using charLES and VPM codes.

we suspect the stratification to be the driving factor for a shorter wavelength, we further investigate the effect of our simulation setup and numerics.

#### 4.2. Vortex descent rate and separation distance

We compare the vortex descent rates between the baseline and forced vortex sheet cases and across codes in Figure 1. We observe that the forced cases diverge earlier as they link faster than the corresponding baseline cases. In addition, due to the effect of stratification, the vortices descend slower than the linear descent rate (dashed black line). We note that the vortex linking occurs earlier in the charLES computations than in VPM.

#### 4.3. Distribution of particles

The effect of the ice crystal distribution on the RF is shown in Figure 2. As described in Section 4.1, we observe half the wavelength for the baseline case [two rings forming, Figure 2(a)], whereas, for the forced case, the wavelength corresponds to the forced mode of  $8b_0$  [cf. Figure 2(b)]. This results in a more disperse particle distribution with more warming regions for the latter. The different vortex dynamics lead to a larger particle concentration at the core of the baseline vortex plume and, hence, higher peaks in optical depth. This leads to a cooling effect in terms of RF since the plume can more effectively reflect incoming solar radiation.

The vertical distribution of particle number density is compared in Figure 3. Both codes indicate that the baseline case spreads particles to lower heights. Conversely, the forced case consistently exhibits a bigger bottom lobe.

#### 4.4. Mean particle properties

Throughout this work, we have compared results between the incompressible code VPM and the compressible code charLES. In general, we find a reasonable agreement of the particle properties between codes considering the distinct treatment of density (Boussinesq versus compressible), the differences in numerical methods (vortex method versus finite volume) and interpolation schemes to recover thermodynamic properties at the particle locations. The average growth of the ice crystals between codes is shown in Figure 4(a). While they follow a similar trend, the local peak and valley values differ.

Since we matched the microphysics modeling in simpler cases without gradients, we conclude that the differences in ice crystal growth are mostly due to the temperature, pressure and water vapor fields that are distinct between the compressible and incom-

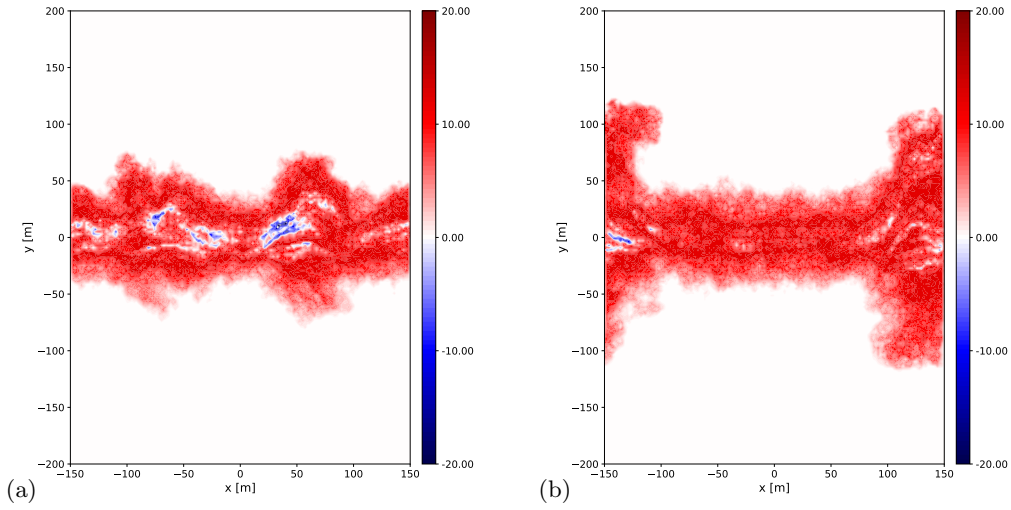


FIGURE 2. Top view of radiative forcing: comparison between (a) the baseline and (b) the forced vortex sheet at a plume age of 225 s using charLES code.

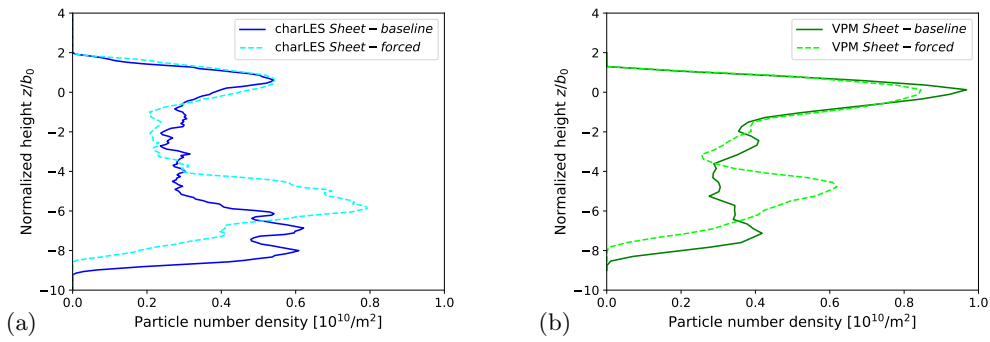


FIGURE 3. Vertical distribution of particles, averaged in the flight direction. Comparison between the baseline and forced vortex sheet at a plume age of 225 s for (a) charLES and (b) VPM.

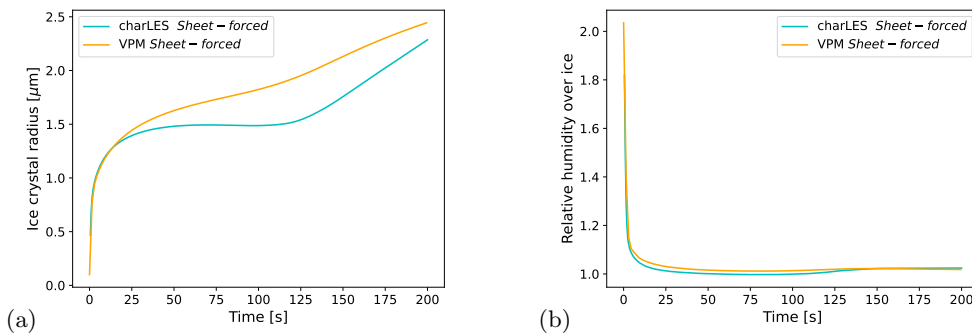


FIGURE 4. Comparison of (a) mean ice crystal radius and (b) mean relative humidity of the particles from the charLES and VPM simulations of the forced vortex sheet case.

pressible code formulations as well as differences in the vortex descent rate and linking time. In spite of these discrepancies, the next section shows that the predictions of the radiative effect of the contrails are consistent.

#### 4.5. Radiative forcing estimates

The RF is estimated through a parameterization based on the optical depth (cf. Section 3). We compare the history of the RE for the baseline and forced vortex sheet cases in Figure 5 for a surface albedo of  $\alpha = 0.2$  and a solar zenith angle of  $\theta = 0^\circ$ , representative of a contrail over land at noon. We observe similar RE values until approximately 15 s; from this time on, distinct particle detrainment causes diverging RF values between the baseline and forced vortex sheet cases.

In general, the forced vortex sheet undergoes an earlier outbreak of the Crow instability and vortex breakdown, leading to a larger RE. The origin of this higher RE can be traced back to the increase in area covered by the plume in the horizontal plane. With an earlier reconnection, the ensuing vortex ring is more potent and carries ice particles away from the center of the plume, locally increasing the lateral extent of the plume as seen from the top. It must be noted that the effect of the ring is to change the spatial distribution at the bottom of the plume, while the particles that were detrained early on (i.e., those concentrating in the top lobe in Figure 3) are unaffected by the dynamics of the vortex reconnection. Since the optical depth is driven by the top particles in the IWP, a change in the lateral extent of the plume has more effect on the RE than a change in the vertical distribution of the particles. The latter could become more influential in the development of the cirrus contrail, but this is out of the scope of the present study.

The observation on the effect of an earlier Crow outbreak holds for the extremes of the surface albedos and solar zenith angles, as shown in Figure 5(a,b,c,d); the maximum impact of the vortex perturbation on the RF is seen over land at noon, whereas the more negligible impact occurs also over land but toward sunset.

## 5. Conclusions

The present investigation showed that, for a given plume representative of a large twin-engine commercial airliner flying in a stably stratified and highly supersaturated atmosphere, forcing the Crow instability leads to an aggravated RF of the contrail for various times of the day and background albedo. This effect on the RF is the largest over land at noon, but remains limited toward sunset over land. The effect of the difference in ice crystal size and spatial distributions on a possibly ensuing cirrus contrail is yet to be determined, which could still possibly lead to a cooling effect through nonlinear feedback of the atmospheric dynamics.

In future work, it would be interesting to investigate the effect of the stratification and jets on the wavelength of the vortex instability, as this leads to a different number of vortex rings between the baseline and forced cases. In addition, jet phase simulations that we ran in parallel of the present effort show an entrainment of the jet closer to a filament resulting in a distinct configuration from a Gaussian plume (as assumed in present work). Therefore, improving the initial conditions of the current vortex simulations with precursor data from the jet phase would result in more representative temperature and water vapor fields as well as soot and ice crystal number and size distributions.

Lastly, a study of the effect of Crow instability for the unstratified configuration would be helpful. Albeit less representative of the atmosphere, the vortex instability wavelength

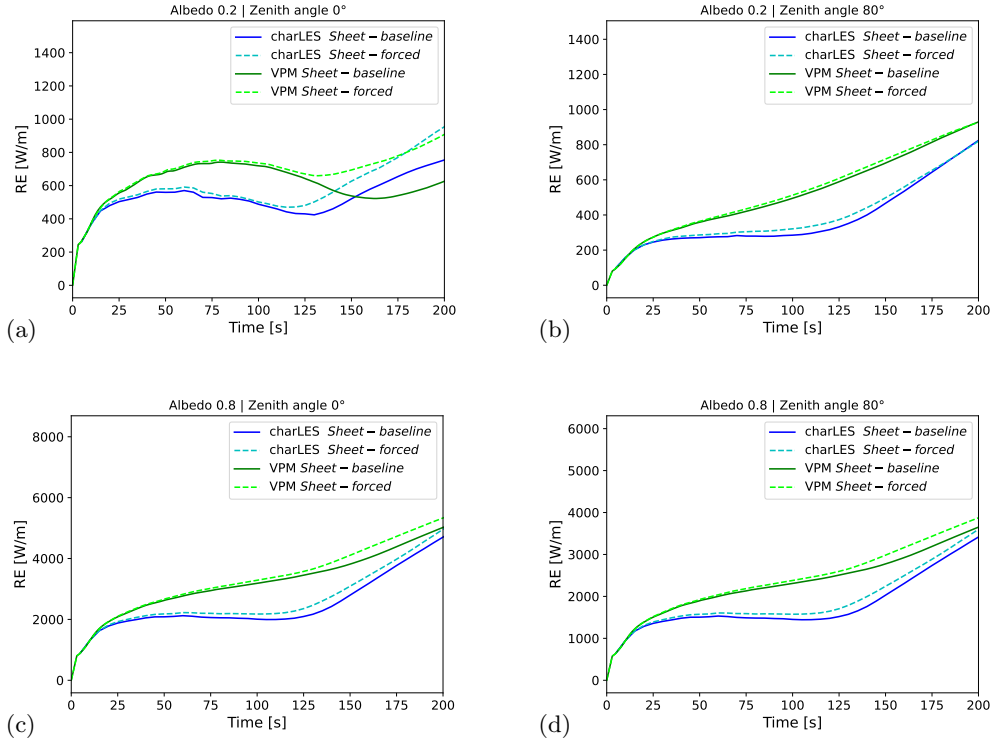


FIGURE 5. Radiative forcing comparison between the baseline and forced vortex sheet and between charLES and VPM codes: (a) over land at noon, (b) over land toward sunset, (c) over snow at noon and (d) over snow toward sunset.

is the same for the baseline and forced cases in the absence of stratification, and the comparison with regards to spatial particle heterogeneity would be more meaningful.

#### Acknowledgments

The authors acknowledge use of computational resources from the Yellowstone cluster awarded by the National Science Foundation to CTR and from the NASA High-End Computing (HEC) Program awarded through the NASA Advanced Supercomputing (NAS) Division at NASA Ames Research Center. The authors also express their deep gratitude to Profs. Philippe Chatelain and Grégoire Winckelmans (UCLouvain, Belgium) for providing access to the source code of VPM4x.

#### REFERENCES

- APPLEMAN, H. 1953 The formation of exhaust condensation trails by jet aircraft. *B. Am. Metereol. Soc.* **34**, 14–20.
- BATCHELOR, G. 1967 *An Introduction to Fluid Dynamics*. Cambridge University Press.
- BICKEL, M., PONATER, M., BOCK, L., BURKHARDT, U. & REINEKE, S. 2020 Estimating the effective radiative forcing of contrail cirrus. *J. Climate* **33**, 1991–2005.
- BIER, A., UNTERSTRASSER, S. & VANCASSEL, X. 2022 Box model trajectory studies of

- contrail formation using a particle-based cloud microphysics scheme. *Atmos. Chem. Phys.* **22**, 823–845.
- BOCK, L. & BURKHARDT, U. 2016 Reassessing properties and radiative forcing of contrail cirrus using a climate model. *J. Geophys. Res.-Atmos.* **121**, 9717–9736.
- CHATELAIN, P., CURIONI, A., BERGDORF, M., ROSSINELLI, D., ANDREONI, W. & KOUMOUTSAKOS, P. 2008 Billion vortex particle Direct Numerical Simulations of aircraft wakes. *Comput. Method. Appl. M.* **197**, 1296–1304.
- CORTI, T. & PETER, T. 2009 A simple model for cloud radiative forcing. *Atmos. Chem. Phys.* **9**, 5751–5758.
- CROUCH, J. D., MILLER, G. D. & SPALART, P. R. 2001 Active-control system for breakup of airplane trailing vortices. *AIAA J.* **39**, 2374–2381.
- CROW, S. 1970 Stability theory for a pair of trailing vortices. *AIAA J.* **8**, 2172–2179.
- HAM, F., MATTSSON, K. & IACCARINO, G. 2006 Accurate and stable finite volume operators for unstructured flow solvers. *Annual Research Briefs*, Center for Turbulence Research, Stanford University, pp. 243–261.
- KÄRCHER, B., MAYER, B., GIERENS, K., BURKHARDT, U., MANNSTEIN, H. & CHATTERJEE, R. 2009 Aerodynamic contrails: Microphysics and optical properties. *Journal of the Atmospheric Sciences* **66**, 227–243.
- LEE, D. S., FAHEY, D. W., SKOWRON, A., ALLEN, M. R., BURKHARDT, U., CHEN, Q., DOHERTY, S. J., FREEMAN, S., FORSTER, P. M., FUGLESTVEDT, J. *et al.* 2021 The contribution of global aviation to anthropogenic climate forcing for 2000 to 2018. *Atmos. Environ.* **244**, 117834.
- LEWEKE, T., LE DIZÈS, S. & WILLIAMSON, C. H. 2016 Dynamics and instabilities of vortex pairs. *Annu. Rev. Fluid Mech.* **48**, 507–541.
- LEWELLEN, D. C. & LEWELLEN, W. S. 2001 The effects of aircraft wake dynamics on contrail development. *J. Atmos. Sci.* **58**, 390–406.
- NAIMAN, A. D. 2011 *Modeling aircraft contrails and emission plumes for climate impacts*. Ph.D. Dissertation, Stanford University.
- PAOLI, R., NYBELEN, L., PICOT, J. & CARIOLLE, D. 2013 Effects of jet/vortex interaction on contrail formation in supersaturated conditions. *Phys. Fluids* **25**, 053305.
- SANZ-MORÈRE, I., EASTHAM, S. D., ALLROGGEN, F., SPETH, R. L. & BARRETT, S. R. H. 2021 Impacts of multi-layer overlap on contrail radiative forcing. *Atmos. Chem. Phys.* **21**, 1649–1681.
- VAN DE HULST, H. C. 1981 *Light scattering by small particles*. Courier Corporation.